Buildup of Fano resonances in the time domain in a double quantum dot Aharonov-Bohm interferometer

Pei-Yun Yang[1,2,*] and Wei-Min Zhang[1,†]

[1]*Department of Physics and Center for Quantum information Science, National Cheng Kung University, Tainan 70101, Taiwan*
[2]*Physics Division, National Center for Theoretical Sciences, National Tsing Hua University, Hsinchu 30013, Taiwan*

In this paper, we investigate the transient quantum transport in a nanoscale Aharonov-Bohm interferometer consisting of laterally coupled double quantum dots (DQDs) coupled to the source and drain electrodes. The transient linear conductance is derived at arbitrary temperature of the leads. The resulting transient conductance can be divided into three terms contributed from different transport channels. From the transient linear conductance and the reduced density matrix elements of the DQD system, we show the buildup of Fano resonances in the time domain.

I. INTRODUCTION

Fano resonance [1] is a universal phenomenon throughout nuclear, atomic, molecular, and optical physics, as well as in various condensed matter systems [2]. It is induced by interference of transport in alternative paths when a discrete state interacts with a continuum sharing the same energy. As distinct from Breit-Wigner resonance [3], which arises due to countertransport in the same quantum path and displays a Lorentz line shape, Fano resonance shows an asymmetric line profile that has both constructive and destructive interference around the resonance energy. A decade ago, with the advent of femtosecond laser, the time-dependent formation of asymmetric Fano line shapes in absorption spectra for a photonionization process was proposed for pump-probe experiments [4]. Until very recently, such a proposal has been verified experimentally in the prototype system of helium [5].

On the other hand, recent experimental developments allow one to measure transient quantum transport in different nano and quantum devices [6–9], thus the buildup of Fano resonance resolved in time in solid-state electronic systems is also of great interest. In fact, Fano effects have been observed in many novel solid state systems, such as open quantum dots [10–13], Aharonov-Bohm (AB) interferometers [14–16], two-dimensional (2D) electronic waveguides and nanotubes [17], where alternative electronic paths can be achieved. Among which, the first tunable Fano resonance is observed in an AB interferometer containing a quantum dot in one of the two arms [15,16], with the benefit that the width (Γ) and Fano factor (q) of Fano resonance are controllable by the AB phase.

Inspired by the experimental realization of the double quantum dots (DQDs) embedded into opposite arms of an AB interferometer [18–20], several works have predicted Fano resonance in this system without [21–26] and with [27–29] Coulomb interactions. In particular, Kang and Cho [23]

revealed analytically that in the double quantum dot AB interferometer, there are two resonances in the steady-state electron conductance at zero temperature near the bonding and antibonding states, which are composed of a Breit-Wigner resonance and a Fano resonance. Furthermore, Kubo *et al.* [26] studied the associated resonances with varying the indirect coupling between double dots through the leads, and they found that Fano resonance can be suppressed as the indirect coupling strength decreases, which remains two Breit-Winger peaks in the steady-state conductance. In this paper, we investigate the transient quantum transport though a double quantum dot AB interferometer to explore how Fano resonance is built up in the time domain in electronic systems.

Using the quantum transport theory based on the master equation approach [30–32], we are able to investigate the transient quantum transport in these novel solid-state systems and also to explore the buildup of Fano resonance in the time domain. We derive the transient linear conductance and the reduced density matrix elements not only at zero temperature but also at finite temperatures. In the situation of a symmetric setup of the double quantum dot AB interferometer, the conductance can be divided into three terms which correspond, respectively, to electrons transport through the bonding and the antibonding channels and the interference between these two channels. By observing the time evolution of each term contributing to the linear conductance, we obtain the different time scales for the formation of Fano resonance and Breit-Wigner resonance. Moreover, we investigate the influence of thermal effects on the time scales to the formation of the resonances and on the resonance profiles. We also compute the time evolution of the reduced density matrix elements of the DQD system. The results help us to understand the nature of the formation of different resonances through the transient quantum transport processes. Also, our results reproduce the steady-state outcomes that have been obtained at zero temperature in the previous works [21–26]. We expect that these transient quantum transport properties on the buildup of Fano resonance in the time domain can be practically observed in experiments.

*l28001177@gmail.com
†wzhang@mail.ncku.edu.tw

The rest of the paper is organized as follows. The setup of the system and the transient linear conductance in the system of a double quantum dot AB interferometer are presented in Sec. II. The transient dynamics of the linear conductance and the corresponding reduced density matrix of the DQD system in the molecular basis are investigated in Sec. III. The time scale of the formation of Fano resonance is obtained. Also, the relation between the resonances and the reduced density matrix is explored. Finally, a summary is presented in Sec. IV. The transient transport theory based on the master equation approach that is used in this work is summarized in the Appendix.

II. TRANSIENT LINEAR CONDUCTANCE AND REDUCED DENSITY MATRIX OF THE DOUBLE QUANTUM DOTS

A. Double quantum dot AB interferometer

The Hamiltonian of a nanoscale AB interferometer consisting of two coupled single-level QDs coupled to two leads is given by

$$
\begin{aligned}
H &= H_{\mathrm{DQD}} + H_E + H_T \\
&= \sum_{i=1}^{2} \varepsilon_{ij} d_i^\dagger d_j + \sum_{\alpha=L,R} \sum_k \epsilon_{\alpha k} c_{\alpha k}^\dagger c_{\alpha k} \\
&\quad + \sum_{\alpha=L,R} \sum_{i=1}^{2} \sum_k (V_{i\alpha k} d_i^\dagger c_{\alpha k} + \mathrm{H.c.}),
\end{aligned}
\tag{1}
$$

where H_{DQD} and H_E are, respectively, the Hamiltonian of the DQDs and the two leads, and d_i ($d_i^\dagger$) and $c_{\alpha k}$ ($c_{\alpha k}^\dagger$) are correspondingly the annihilation (creation) operators of electrons in the ith dot and the kth level in lead α, with ε_{ij} and $\epsilon_{\alpha k}$ being the corresponding energy. The Hamiltonian H_T describes the tunnelings between the dots and the leads, in which $V_{i\alpha k} = \bar{V}_{i\alpha k} e^{i\phi_{i\alpha}}$ with the phase coming from the magnetic flux Φ threading into the AB ring. It gives $\phi_{1L} - \phi_{1R} + \phi_{2R} - \phi_{2L} = 2\pi\Phi/\Phi_0 = \varphi$, where Φ_0 is the flux quanta. Here, we focus on the single-particle interference properties and disregard Coulomb interactions, which can be done by controlling the energy scale of the nanodevice to let the interdot Coulomb correlations become negligible and to set up the DQDs in the Coulomb blockage regime for practical applications.

In order to study the resonance dynamics in the double-dot AB interferometer, we may express the DQDs in the molecular basis by diagonalizing H_{DQD}. Denoting the bonding state and the antibonding state of the DQD molecule with the signs $-$ and $+$, respectively, the Hamiltonian of the DQDs becomes

$$
H_{\mathrm{DQD}} = \sum_{\nu=\pm} \varepsilon_\nu d_\nu^\dagger d_\nu.
\tag{2}
$$

Without loss of generality, we can let the energy of each dot $\varepsilon_{11} = \varepsilon_{22} = \varepsilon_0$ and the tunneling matrix between the two dots $\varepsilon_{12} = \varepsilon_{21} = -t_c$. Then, $\varepsilon_\pm = \varepsilon_0 \pm t_c$ are the corresponding

energy levels of the molecular states, and $d_\pm$ ($d_\pm^\dagger$) are the associated annihilation (creation) operators, which are given by:

$$
\begin{pmatrix} d_+ \\ d_- \end{pmatrix} = \frac{1}{\sqrt{2}} \begin{pmatrix} 1 & -1 \\ 1 & 1 \end{pmatrix} \begin{pmatrix} d_1 \\ d_2 \end{pmatrix}.
\tag{3}
$$

The tunneling Hamiltonian between the molecular states and the leads is transformed accordingly,

$$
H_T = \sum_{\alpha=L,R} \sum_{\nu=\pm} \sum_k (V_{\nu\alpha k} d_\nu^\dagger c_{\alpha k} + \mathrm{H.c.}),
\tag{4}
$$

with the tunneling matrix elements,

$$
\begin{pmatrix} V_{+\alpha k} \\ V_{-\alpha k} \end{pmatrix} = \frac{1}{\sqrt{2}} \begin{pmatrix} 1 & -1 \\ 1 & 1 \end{pmatrix} \begin{pmatrix} V_{1\alpha k} \\ V_{2\alpha k} \end{pmatrix}.
\tag{5}
$$

Meanwhile, in order to observe a distinct feature of Fano resonance, one needs to prepare a constant background coupled to a discrete level. Therefore, we take the spectral density of lead α in Eq. (A5) to be energy independent, $\mathbf{\Gamma}_\alpha(\omega) = \mathbf{\Gamma}_\alpha$ (corresponding to the wide band limit) with the asymmetric level widths of the left lead $\Gamma_{L11} = \Gamma_{L22} = \Gamma_L$ and the right lead $\Gamma_{R11} = \Gamma_{R22} = \Gamma_R$. Also the indirect interdot couplings through the left lead $\Gamma_{L12} = \Gamma_L e^{i\frac{\varphi}{2}}$ and the right lead $\Gamma_{R12} = \Gamma_R e^{-i\frac{\varphi}{2}}$. As a result, the level-width matrix $\mathbf{\Gamma}_\alpha$ in the molecular basis is given by

$$
\begin{pmatrix} \Gamma_{++} & \Gamma_{+-} \\ \Gamma_{-+} & \Gamma_{--} \end{pmatrix}_{L,R} = \Gamma_{L,R}(\mathbf{1} - \vec{\alpha}_{L,R} \cdot \vec{\boldsymbol{\sigma}}),
\tag{6}
$$

where $\vec{\alpha}_{L,R} = (\alpha_{L,R}^x, \alpha_{L,R}^y, \alpha_{L,R}^z) = (0, \pm\sin\frac{\varphi}{2}, \cos\frac{\varphi}{2})$ and $\vec{\boldsymbol{\sigma}}$ are the Pauli matrices. It shows that the level width in the molecular basis is effectively controlled by the AB phase φ, which is an equivalent realization of asymmetric couplings between the double dots and the two leads.

B. Transient linear conductance and reduced density matrix in the molecular basis of the DQDs

The buildup of Fano resonance in the time domain is manifested in the transient linear conductance. The transient linear conductance is defined as

$$
\mathcal{G}(t) = \frac{\partial}{\partial V} I(t)|_{V=0},
\tag{7}
$$

where $I(t) = 1/2[I_L(t) - I_R(t)]$ is the transient net transport current and $\mu_{L,R} = E_F \pm eV/2$, in which E_F denotes the Fermi level of the leads and V is the bias applied to the two leads. We use the quantum transport theory based on the master equation approach [30–32] to explore the transient features of the linear conductance. The explicit form of the exact master equation for the given total Hamiltonian (1) and the corresponding transient current derived from the master equation are summarized in the Appendix, see Eqs. (A1), (A10), and (A11). From Eq. (A11), one can find explicitly the transient linear conductance in the wide band limit,

$$
\begin{aligned}
\mathcal{G}(t) = -\frac{e^2}{h}\mathrm{ReTr}\Bigg\{ &\frac{1}{4}(\mathbf{\Gamma}_L - \mathbf{\Gamma}_R) \int_{t_0}^t d\tau_1 \int_{t_0}^t d\tau_2 \, \boldsymbol{u}(t,\tau_1)(\mathbf{\Gamma}_L - \mathbf{\Gamma}_R) \int d\omega \frac{\beta/2}{1+\cosh[\beta(\omega-E_F)]} e^{-i\omega(\tau_1-\tau_2)} \boldsymbol{u}^\dagger(t,\tau_2) \\
&- \frac{1}{2}(\mathbf{\Gamma}_L + \mathbf{\Gamma}_R) \int_{t_0}^t d\tau \int d\omega \frac{\beta/2}{1+\cosh[\beta(\omega-E_F)]} e^{-i\omega(t-\tau)} \boldsymbol{u}^\dagger(t,\tau) \Bigg\},
\end{aligned}
\tag{8}
$$

where the retarded Green function $\boldsymbol{u}(t,\tau)$ has the following solution,

$$\boldsymbol{u}(t,\tau) = \exp\left[-\left(i\boldsymbol{\varepsilon} + \tfrac{1}{2}\boldsymbol{\Gamma}\right)(t-\tau)\right], \qquad (9)$$

and $\boldsymbol{\varepsilon} = \begin{pmatrix} \varepsilon_+ & 0 \\ 0 & \varepsilon_- \end{pmatrix}$ and $\boldsymbol{\Gamma} = \boldsymbol{\Gamma}_L + \boldsymbol{\Gamma}_R$. Note that the transient liner conductance is independent of the initial state of the DQDs. This is because the DQD initial-state dependence in the transient net current, the first term in Eq. (A11) is independent of the bias voltage. Therefore, according to the definition of the transient linear conductance Eq. (7), the derivative to the bias voltage makes this initial-state dependence vanish in $\mathcal{G}(t)$.

When the leads are initially at zero temperature ($\beta \to \infty$), the frequency dependent term in Eq. (8) is reduced to a delta function: $\frac{\beta/2}{1+\cosh[\beta(\omega - E_F)]} \to \delta(\omega - E_F)$. In the steady-state limit ($t \to \infty$), one can then reproduce the linear conductance obtained previously in Refs. [21–26],

$$\mathcal{G} = \frac{e^2}{h} \mathrm{Tr}[\boldsymbol{\Gamma}_L \boldsymbol{G}^R(E_F) \boldsymbol{\Gamma}_R \boldsymbol{G}^A(E_F)], \qquad (10)$$

where the retarded Green function in energy domain,

$$\mathbf{G}^R(E_F) = -i \lim_{t \to \infty} \lim_{t_0 \to -\infty} \int_{t_0}^{t} e^{iE_F(t-\tau)} \boldsymbol{u}(t,\tau) d\tau,$$

$$= \left(E_F \boldsymbol{I} - \boldsymbol{\varepsilon} + \frac{i}{2}\boldsymbol{\Gamma}\right)^{-1}, \qquad (11)$$

and the advanced Green function $\mathbf{G}^A(E_F) = [\mathbf{G}^R(E_F)]^\dagger$. Also, we have used the relation $\mathbf{G}^R(E_F) - \mathbf{G}^A(E_F) = -i\mathbf{G}^R(E_F)\boldsymbol{\Gamma}\mathbf{G}^A(E_F)$ [33–35] in obtaining Eq. (10).

On the other hand, in the molecular basis, the quantum states of the DQD system, described by the reduced density matrix elements $\rho_{\nu\nu'}(t)$ that obey the master equation (A1) for an arbitrary initial DQD state, can be expressed as [36] (also see Appendix)

$$\rho_{00}(t) = A(t)\Bigg\{\rho_{00}(t_0) + \rho_{dd}(t_0)\det[\boldsymbol{J}_3(t)]$$

$$- \sum_{\nu,\nu'=\pm} \rho_{\nu\nu'}(t_0) \boldsymbol{J}_{3\nu'\nu}(t)\Bigg\}, \qquad (12a)$$

$$\rho_{++}(t) = 1 - \rho_{00}(t) - \rho_{--}^{(1)}(t), \rho_{+-}(t) = \rho_{+-}^{(1)}(t), \quad (12b)$$

$$\rho_{--}(t) = 1 - \rho_{00}(t) - \rho_{++}^{(1)}(t), \rho_{-+}(t) = \rho_{+-}^{*}(t), \quad (12c)$$

$$\rho_{dd}(t) = 1 - \rho_{00}(t) - \rho_{++}(t) - \rho_{--}(t), \qquad (12d)$$

where $A(t), \boldsymbol{J}_3(t)$ are given explicitly after Eq. (A7) in the Appendix. $\rho_{\nu\nu'}^{(1)}(t) = \rho_{\nu\nu'}^{(1)}(t,t) = \langle a_{\nu'}^\dagger(t) a_\nu(t)\rangle$ is the single particle density matrix, which is the single particle correlation function at the same time ($\tau = t$) given explicitly by Eq. (A8). It is shown that all these quantities are fully determined by the retarded Green function $\boldsymbol{u}(t,\tau)$ [see Eq. (9)] through the correlation Green function of Eq. (A6) in the nonequilibrium Green function technique. If the dots are initially in an empty state, the elements of the reduced density matrix are simplified to

$$\rho_{00}(t) = \det[\mathbf{1} - \boldsymbol{v}(t,t)], \qquad (13a)$$

$$\rho_{++}(t) = 1 - \rho_{00}(t) - \boldsymbol{v}_{--}(t,t), \rho_{+-} = \boldsymbol{v}_{+-}(t,t), \quad (13b)$$

$$\rho_{--}(t) = 1 - \rho_{00}(t) - \boldsymbol{v}_{++}(t,t), \rho_{-+} = \boldsymbol{v}_{+-}^{*}(t,t), \quad (13c)$$

$$\rho_{dd} = \det[\boldsymbol{v}(t,t)]. \qquad (13d)$$

Thus, the reduced density matrix elements of the DQDs are simply determined by the correlation Green function $\boldsymbol{v}(t,t)$ [the solution is given by Eq. (A6) in the Appendix] which can be easily derived from Eq. (9). In other words, both the transient linear conductance in this double-dot AB interferometer and the time evolution of the reduced density matrix of the DQDs are fully determined by the retarded Green function $\boldsymbol{u}(t,\tau)$ of Eq. (9) with the level width $\boldsymbol{\Gamma}_{L,R}$ of Eq. (6) and therefore can be manipulated by varying the AB phase φ, as we will show in the next sections.

III. BUILDUP OF FANO RESONANCE IN THE TIME DOMAIN

A. Steady-state Fano resonance

To get an instructive physical picture, we shall present first the steady-state results of Fano resonance in this double-dot AB interferometer. We focus on the case of a symmetric geometry $\Gamma_L = \Gamma_R = \Gamma/2$, without loss of generality. This is because the resonances can be manipulated by the AB phase φ through the applied magnetic flux, which equivalently generates various asymmetric geometries of the DQDs with respect to the molecular basis, see Eq. (6) and the results given below. Then, according to Eq. (10), the steady-state linear conductance at zero temperature is explicitly given by

$$\mathcal{G} = \frac{e^2}{h} \frac{(e_+ - e_-)^2}{(e_+^2 + 1)(e_-^2 + 1)}. \qquad (14)$$

The dimensionless energies $e_{+,-} \equiv (E_F - \varepsilon_{+,-})/(\Gamma_{+,-}/2)$, with $\Gamma_+ = \Gamma_{L++} + \Gamma_{R++} = 2\Gamma \sin^2(\varphi/4)$ and $\Gamma_- = \Gamma_{L--} + \Gamma_{R--} = 2\Gamma \cos^2(\varphi/4)$ which depend explicitly and sensitively on the AB phase φ. Equation (14) reproduces the results in Ref. [23] and reveals two resonances, a Breit-Wigner resonance and a Fano resonance, when the bandwidth of the two molecular states $\Gamma_+ \gg \Gamma_-$ or $\Gamma_- \gg \Gamma_+$. Explicitly, when $\Gamma_+ \gg \Gamma_-$, in the energy scale near the antibonding state energy ($|e_-| \gg 1$), the conductance of Eq. (14) follows the Breit-Wigner form of its width $\Gamma_+/2$ [23]:

$$\mathcal{G} \simeq \frac{e^2}{h} \frac{1}{e_+^2 + 1}. \qquad (15)$$

While in the energy scale near the bonding state energy ($|e_-| \lesssim 1$), one can find that the conductance shows Fano resonance profile:

$$\mathcal{G} \simeq \frac{e^2}{h} \frac{1}{q^2 + 1} \frac{(e_- + q)^2}{e_-^2 + 1}, \qquad (16)$$

where the Fano factor $q = 4t_c/\Gamma_+$ which is the ratio of the interdot coupling and the level broadening of the antibonding state. Hence, the conductance is composed of a Breit-Wigner resonance at the antibonding state energy and a Fano resonance near the bonding state energy. If one takes $\Gamma_- \gg \Gamma_+$, the same analysis is applied with the role of the bonding and antibonding states interchanged with the Fano factor given by $q = -4t_c/\Gamma_-$.

To get a better understanding of the electron transport behavior through different paths, we can divide the linear conductance Eq. (10) into components flowing through the bonding and antibonding state channels, plus the interference
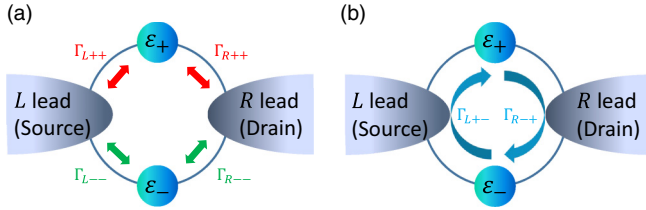
FIG. 1. Different paths for electron transport between the source and drain through the molecular states. (a) Electrons countertransport through bonding and antibonding channels, respectively. (b) Electrons transport through both bonding and antibonding channels.

of electron transport through different paths in the AB ring geometry,

$$\mathcal{G} = \mathcal{G}_+ + \mathcal{G}_- + \mathcal{G}_{+-}. \quad (17)$$

Each component is given explicitly by

$$\mathcal{G}_\pm = \frac{e^2}{h} \Gamma_{L\pm\pm} \Gamma_{R\pm\pm} |G^R_{\pm\pm}(E_F)|^2 = \frac{e^2}{h} \frac{1}{e_\pm^2 + 1}, \quad (18a)$$

$$\mathcal{G}_{+-} = 2\frac{e^2}{h} \mathrm{Re}\{\Gamma_{L+-} G^R_{--} \Gamma_{R-+} G^A_{++}\}$$

$$= -\frac{e^2}{h} \frac{2(e_+ e_- + 1)}{(e_+^2 + 1)(e_-^2 + 1)}, \quad (18b)$$

where $\mathcal{G}_\pm$ are, respectively, conductances of electrons counterflowing through the bonding and antibonding state channels, as shown in Fig. 1(a), which give two Breit-Wigner resonances in the electron conductance. On the other hand, because there is no direct coupling between the bonding and antibonding states [Green function $\boldsymbol{u}(t, t_0)$ is diagonal], $\mathcal{G}_{+-}$ describes the interference between electron transport through bonding and antibonding channels, induced by the indirect interdot coupling through the two leads as shown in Fig. 1(b). This interference leads to Fano resonance. Thus, it is obvious that when there is no indirect interdot coupling, Fano resonance will be suppressed, which results in two Breit-Winger peaks in the steady-state conductance as shown in Ref. [26].

Figure 2 shows the conductances as a function of Fermi energy of the leads for different values of the AB phase φ. Here the AB phase solely determines the bandwidth $\Gamma_\pm$ and the Fano factor q when one fixes the interdot coupling t_c. One can see that conductance terms $\mathcal{G}_+$ and $\mathcal{G}_-$ contribute two Breit-Winger peaks at the antibonding and bonding energies $\varepsilon_\pm$, as discussed above. Meanwhile, the interference term $\mathcal{G}_{+-}$ is very sensitive to the AB phase φ. For $\varphi = 0.3\pi$ for an example, $\Gamma_- > \Gamma \gg \Gamma_+$. Correspondingly, the interference term makes, respectively, a constructive and a destructive contribution to the resonance transport when the Fermi energy E_F approaches the antibonding state energy $\varepsilon_+ = \Gamma$ (here we take $\varepsilon_0 = 0$) from the left and the right sides, see the first plot in Fig. 2. This interference induces a Fano resonance at the antibonding state energy in the total conductance. As a result, the total conductance of the system shows a Breit-Wigner resonance at the bonding state energy and a Fano resonance at the antibonding state energy, as shown in Fig. 2(a). When the AB phase φ changes, for example, $\varphi = 0.7\pi$, the interference term $\mathcal{G}_{+-}$ still leads to Fano resonance at the antibonding
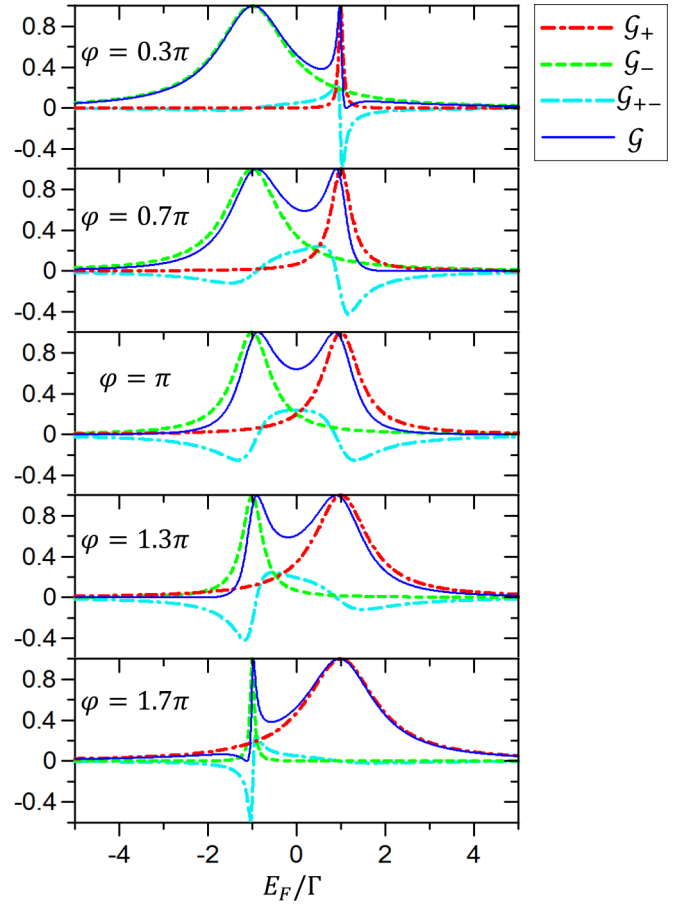

FIG. 2. Components of steady linear conductance at zero temperature as a function of Fermi energy for different values of the AB phase φ, where $\varepsilon_0 = 0$, $t_c = \Gamma$.

state except that Fano factor q gets larger because of the smaller Γ_-. In the meantime, the Breit-Wigner resonance at the bonding state energy gradually grows into a Fano-like resonance (asymmetric resonance), see Fig. 2(b). When $\varphi = \pi$, $\Gamma_- = \Gamma_+ = \Gamma$, the interference term $\mathcal{G}_{+-}$ is symmetric with the Fermi energy E_F. Correspondingly, both resonances around the bonding and antibonding state energies become Fano resonances with Fano factor $q \simeq -4$ and $q \simeq 4$ in the total conductance, respectively. For the other case of the AB phase $\varphi = 1.7\pi$, we have $\Gamma_+ > \Gamma \gg \Gamma_-$. Then the role of the bonding and antibonding states interchanges. As a result, the conductance consists of a Breit-Wigner resonance at the antibonding state energy and a Fano resonance at the bonding state energy.

As one can see, the results in Fig. 2 indicate that the AB phase φ plays an effective role to equivalently generate various asymmetric geometries of the DQDs in the molecular basis and also effectively covers the exchange symmetry of molecular states. In fact, the results of Fig. 2 also manifest the phase rigidity of the steady-state transport conductance in the quantum dot AB interferometer, as one expected [37–40].

B. Buildup of Fano resonance in the time domain

After examining the above general steady-state resonant behaviors, we now explore the real-time dynamics of the
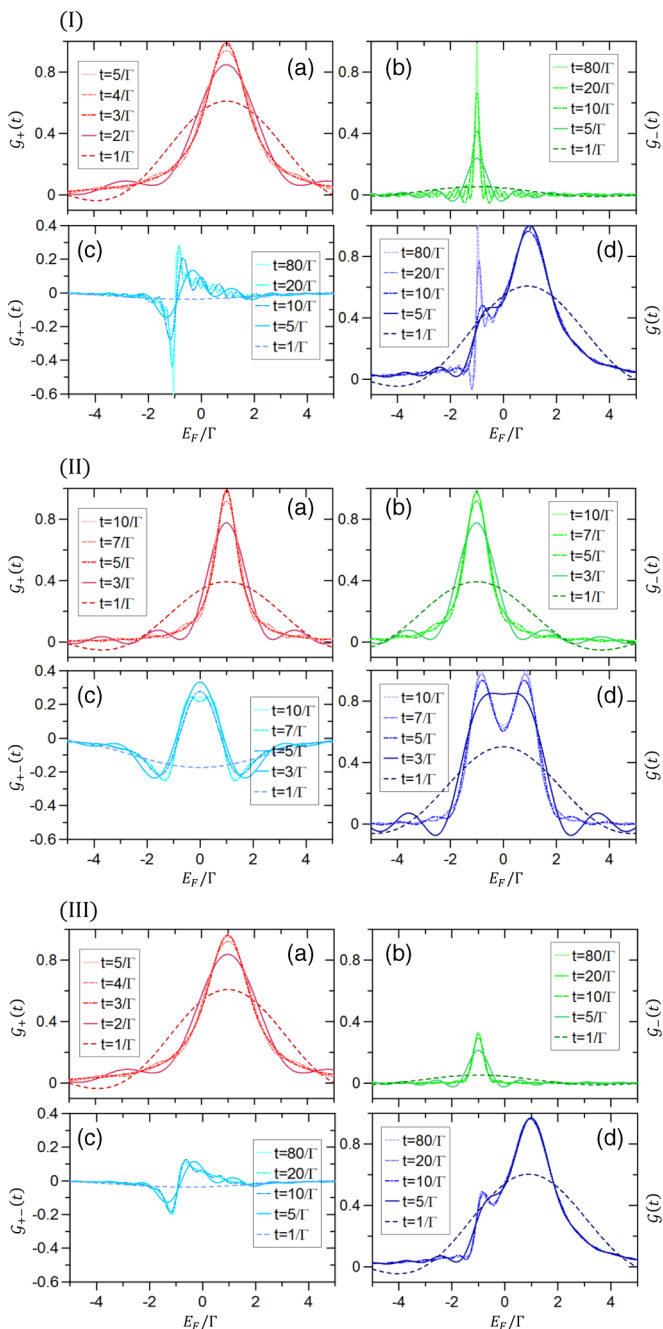
FIG. 3. Time evolution of the components of linear conductance as a function of Fermi energy at zero temperature for (I) $\varphi = 1.7\pi$ and (II) $\varphi = \pi$ and (III) at initial temperature of the leads $k_B T = 0.1\Gamma$ for $\varphi = 1.7\pi$, where $\varepsilon_0 = 0$, $t_c = \Gamma$.

buildup of Fano resonance. We set $t_0 = 0$ hereafter. The time evolution of the transient linear conductance at zero temperature with the AB phase $\varphi = 1.7\pi$ ($\Gamma_+ > \Gamma \gg \Gamma_-$) is displayed in Fig. 3(I). At the beginning ($t = 1/\Gamma$), because the coupling of the antibonding state to the two leads is much larger than that of the bonding state, electrons mainly transport to the antibonding state, although its energy is higher than that of the bonding state. As one can see from Fig. 3(I), when $t = 1/\Gamma$, the component $\mathcal{G}_+$ grows fast and forms a resonance at the antibonding state energy, while $\mathcal{G}_-$ and $\mathcal{G}_{+-}$ are almost zero.

As time increases, $\mathcal{G}_+$ rapidly steadies to a Breit-Winger resonance with full transmission at the antibonding state energy with $t < 5/\Gamma$, see Fig. 3(I)(a). The time scale to reach the steady state for the Breit-Wigner resonance can be found from the Green function component $u_{++}(t, t_0)$. It is proportional to the inverse of the decay rate $\Gamma_+/2$ in $u_{++}(t, t_0)$ [see Eq. (9)]. On the other hand, the steady state of $\mathcal{G}_-$ and $\mathcal{G}_{+-}$ is reached in the scale of the inverse of the decay rate $\Gamma_-/2$. The formation of Fano resonance at the bonding state energy comes from the combination of these two terms in this case. Therefore, the time scale for the formation of the Fano resonance is determined by the effective coupling Γ_- between the bonding state and the two leads, which is much longer than the time scale for the formation of the Breit-Wigner resonance at the antibonding state energy. In Figs. 3(I)–(d), the time evolution of $\mathcal{G}_-$, $\mathcal{G}_{+-}$ and the total conductance $\mathcal{G}$ is presented, and as one can see the Fano resonance is fully built up around $t \simeq 80/\Gamma$, where the interference pattern combines both the full constructive and destructive interferences.

Concerning the possible effects on Fano resonance from various symmetries in the flux dependence discussed in the beginning of this section, we take the most symmetric case with AB phase $\varphi = \pi$ as an example. In this case, $\Gamma_+ = \Gamma_- = \Gamma$, the time evolution of the transient linear conductance at zero temperature is displayed in Fig. 3(II). Because the couplings of the left and the right leads to the molecular states of the DQDs are symmetric, conductances through the bonding and antibonding channels have the same behavior around the resonant energies ε_- and ε_+. As one can see from Fig. 3(II)(a) and Fig. 3(II)(b), $\mathcal{G}_+(t)$ and $\mathcal{G}_-(t)$ are symmetric built up with each other both in the transient and in the steady state regimes. The interference between the two channels and the resulting total conductance are also symmetric with Fermi energy E_F. The time for reaching the steady state is $t \simeq 10\Gamma$ in this case, see Figs. 3(II)(c)–(d). The result shows that symmetries have not much help in enhancing Fano resonance.

Considering the thermal effect, the transient dynamics of the linear conductance for $\varphi = 1.7\pi$ at initial temperature of the leads $k_B T = 0.1\Gamma$ is shown in Fig. 3(III), in comparison with the zero-temperature case of Fig. 3(I). For the conductance through the antibonding channel [Fig. 3(III)(a)], the result is almost the same as that in the zero temperature case [Fig. 3(I)(a)], except that the transmission at the antibonding energy is slightly decreased due to the thermal effect. In this case, the level width of the antibonding state $\Gamma_+/2 \simeq 0.95\Gamma$ (for $\varphi = 1.7\pi$) still dominates the damping, while the temperature-induced level broadening is proportional to $k_B T = 0.1\Gamma$. Hence, the resonant transport through the antibonding channel, i.e. the Breit-Wigner resonance, is less affected by thermal broadening effect. For the conductance of electrons passing the bonding channel and the electron interference between the bonding and antibonding channels, see Fig. 3(III)(b) and 3(III)(c), the resonant behavior depends mainly on level width $\Gamma_-/2 \simeq 0.05\Gamma$ (for $\varphi = 1.7\pi$) which is less than the thermal broadening effect ($k_B T = 0.1\Gamma$). Therefore, the amplitudes of the resonance peak of $\mathcal{G}_-$ and the conductance $\mathcal{G}_{+-}$ are significantly suppressed by the thermal effect. Moreover, the time to the steady state values of conductance $\mathcal{G}_-$ and $\mathcal{G}_{+-}$ is also largely reduced due to the thermal fluctuations: $t \simeq 20\Gamma$, in comparison with $t \simeq 80\Gamma$ in the zero temperature case. As
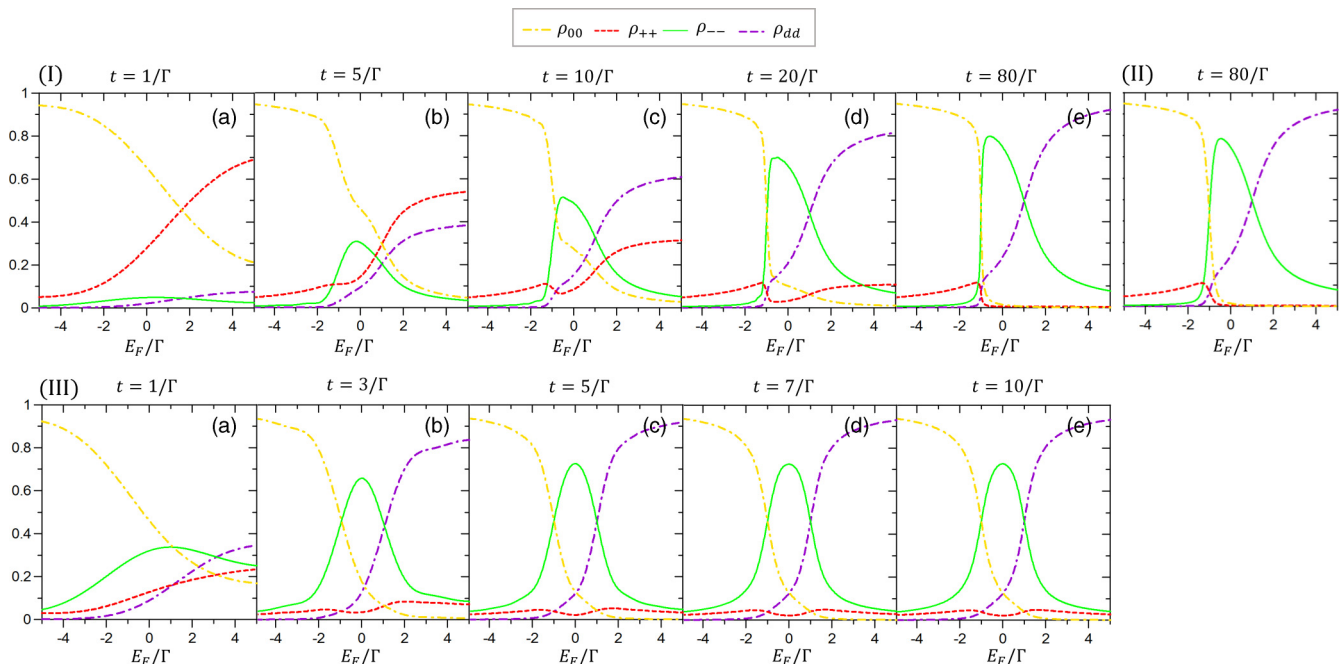
FIG. 4. Time evolution of the reduced density matrix elements of the DQDs at zero temperature for (I) $\varphi = 1.7\pi$ and (III) $\varphi = \pi$. (II) Steady state results of the reduced density matrix elements of the DQDs at the initial temperature of leads $k_B T = 0.1\Gamma$. The system is initially in an empty state, and $\varepsilon_0 = 0$, $t_c = \Gamma$.

a result, the Fano resonance is strongly suppressed as one can see from the total linear conductance $\mathcal{G}$ in Fig. 3(III)(d), where the full constructive and destructive interferences in the Fano resonance are significantly reduced.

C. The electron distributions in the molecular states associated with Fano resonance in terms of the reduced density matrix

To see how the quantum state of the DQD system redistributes when resonances occur, we turn to explore the time evolution of the reduced density matrix of the DQDs. Consider the system initially in an empty state; the elements of the reduced density matrix are given by Eq. (13), which are fully determined by Green function $\boldsymbol{v}(t,t)$. Moreover, we let the leads be unbiased, i.e., $\mu_L = \mu_R = E_F$. In the symmetric setup of the DQDs ($\Gamma_L = \Gamma_R = \Gamma/2$), the off-diagonal terms of the reduced density matrix in the molecular basis are zero because the Green function $\boldsymbol{v}(t,t)$ is diagonal. The transient dynamics of the reduced density matrix at zero temperature with AB phase $\varphi = 1.7\pi$ ($\Gamma_+ > \Gamma \gg \Gamma_-$) is shown in Fig. 4(I). In the beginning ($t = 1/\Gamma$), electron transport is dominated by the couplings between the DQDs and the leads. As E_F varying from negative to positive energy by gate control of the dot energy ε_0, electrons prefer to occupy the antibonding state because of its larger couplings to the leads, so that the empty state probability ρ_{00} is decreased and the antibonding state probability ρ_{++} is increased, while ρ_{--} and ρ_{dd} almost keep to zero. With time going, electrons transporting from the leads to the DQDs also begin to be trapped in the bonding state when $E_F > \varepsilon_-$, which results in an increase of the probability of the doubly occupied state as well. As one can see, later than $t = 5/\Gamma$, ρ_{--} dramatically increases after E_F passing the bonding state energy ε_- and then decreases after reaching a maximum value. This maximum value gets larger with the time

going as shown by the solid green curve in Figs. 4(I)(b)–(e). While the probability of the doubly occupied state ρ_{dd} (the dash-dash-dot purple curve) increases when $E_F > \varepsilon_-$ and keeps climbing with E_F in time.

Eventually, when the total system reaches the steady-state limit ($t \simeq 80/\Gamma$), we can see that in the range $E_F < \varepsilon_-$, the state of the DQD system has the most probability in an empty state ($\rho_{00} \simeq 1$), while there is less probability for electrons to occupy in the antibonding state because of its larger coupling Γ_+ to the leads. As a result, electrons quickly transport through the antibonding state. At $E_F = \varepsilon_-$ ($\varepsilon_- = -\Gamma$ in Fig. 4), there are two strong (rapid) occupation inversions, see Fig. 4(I)(e). One is the probability inversion between the empty state ρ_{00} and the bonding state ρ_{--}; the other one is between the antibonding state ρ_{++} and the doubly occupied state ρ_{dd}. Both of the probability inversions indicate that there is a resonant tunneling from the leads to the bonding state. In the range $E_F > \varepsilon_-$, the probabilities ρ_{00} and ρ_{++} rapidly reduce to zero. As mentioned, the probability ρ_{--} reaches a maximum value and then decreases in larger E_F, while ρ_{dd} keeps climbing with E_F, which leads to a probability inversion between the bonding state and doubly occupied state at $E_F = \varepsilon_+$ ($\varepsilon_+ = \Gamma$ in Fig. 4).

Compared with the transient conductance in Fig. 3(I), we find that resonances occur when the occupation probabilities show an inversion between the states differing with one electron, e.g., $|0\rangle \leftrightarrow |\pm\rangle$ or $|\pm\rangle \leftrightarrow |d\rangle$. Also, it indicates that the Breit-Wigner resonance involves one transition channel, however the Fano resonance involves two channels. In particular, the steady state ($t \simeq 80/\Gamma$) in Fig. 4(I)(e) shows that the Breit-Wigner resonance at antibonding state energy ε_+ presents a probability inversion from ρ_{--} to ρ_{dd}. Fano resonance at bonding state energy ε_- exhibits two probability inversions both from ρ_{00} to ρ_{--} and from ρ_{++} to ρ_{dd}. Moreover the probability inversion rate is determined by the bandwidths.

In this case ($\varphi = 1.7\pi$), the probability inversion with gentle slope (weak) leads to a Breit-Wigner resonance because of its larger bandwidth, whereas the strong probability inversion leads to a Fano resonance corresponding to a much smaller bandwidth. However, when the thermal effect is considered, we find that the strong probability inversion at the bonding state energy is apparently eased off. The steady state results of the reduced density matrix elements at the initial temperature of the leads $k_B T = 0.1\Gamma$ is presented in Fig. 4(II). It shows that the thermal broadening effects smear significantly the Fano resonance, as one expected.

Figure 4(III) shows the transient dynamics of the reduced density matrix at zero temperature under the symmetric coupling to the molecular states, i.e., $\varphi = \pi$ ($\Gamma_+ = \Gamma_- = \Gamma$). Unlike the linear transient conductance shown in Fig. 3(II) which shows a symmetric behavior both in the transient and the steady state regimes, the elements of the reduced density matrix represent asymmetric profiles in the transient regime because of the initial state dependence. With time increasing, the probabilities ρ_{00} and ρ_{dd} become more and more symmetric with each other, and ρ_{--} and ρ_{++} also grow into symmetric profiles in the Fermi energy E_F. In the steady-state limit ($t \simeq 10/\Gamma$), there are two sets of probability inversions between the elements of the reduced density matrix which indicate two Fano resonances; each shows two transition channels with the same bandwidth at the resonant energies ε_- and ε_+. By comparing Figs. 4(I) and 4(III), we also find that the strong and weak probability inversions correspond to the strong and weak asymmetric Fano resonances with smaller and larger Fano factors, respectively. This is indeed the explicit evidence of Fano resonance manifested in the reduced density matrix elements. It is worth mentioning that, when interdot coulomb interaction is included, the probability of the doubly occupied state will be reduced accordingly, which results in the increase of the probability of the single-electron states [41] and certainly will change the occupation inversion.

IV. SUMMARY

In summary, using the quantum transport theory based on the master equation approach [30–32], we obtain the transient linear conductance and the reduced density matrix elements of the DQDs not only at zero temperature but also at finite temperatures. The conductance can be divided into components flowing through the bonding and antibonding state channels, plus the interference component from the mixed channels between them. We investigate the transient dynamics in terms of each component of linear conductance. We find that the time scale for the formation of Fano resonance is much slower than the formation of the Breit-Wigner resonance, because of the large differences of the effective couplings between each molecular level of DQDs and the leads. Also, Fano resonance can be smeared by the thermal effect. From the transient dynamics of the reduced density matrix elements, we find that resonance occurs when the occupation probabilities invert between the states differing by one electron, e.g., $|0\rangle \leftrightarrow |\pm\rangle$ or $|\pm\rangle \leftrightarrow |d\rangle$. The inversion at the resonant energy with one probability channel corresponds to Breit-Wigner resonance, whereas the inversion with two probability channels leads to Fano resonance, as an interference effect. The real-time

interference dynamics through the electron conductance in the double-dot AB interferometer helps us to understand how Fano resonance is built up. We expect such dynamical Fano resonance to be observed in experiments.

APPENDIX: EXACT MASTER EQUATION APPROACH FOR TRANSIENT QUANTUM TRANSPORT

The device described in Hamiltonian (1) can be treated as an open quantum system. The dynamics of the DQD system is described by the reduced density matrix $\rho(t) = \text{Tr}_E[\rho_{\text{tot}}(t)]$, which is obtained by tracing over all the degrees of freedom of the leads from the total density matrix $\rho_{\text{tot}}(t)$ of the DQDs plus the leads. As usual, the DQDs and the leads are considered to be initially decoupled, and the leads are initially in equilibrium states. We have derived the exact master equation which governs the dynamics of $\rho(t)$ for the DQDs [30–32,36,37]:

$$\frac{d\rho(t)}{dt} = -\frac{i}{\hbar}[H'_S(t), \rho(t)] + \sum_{i,j}\{\gamma_{ij}(t)[2d_j\rho(t)d_i^\dagger$$
$$- d_i^\dagger d_j \rho(t) - \rho(t)d_i^\dagger d_j] + \widetilde{\gamma}_{ij}(t)[d_i^\dagger\rho(t)d_j$$
$$- d_j\rho(t)d_i^\dagger + d_i^\dagger d_j\rho(t) - \rho(t)d_j d_i^\dagger]\}. \quad \text{(A1)}$$

The first term of Eq. (A1) describes the unitary evolution of electrons in the device system, where the renormalized Hamiltonian $H'_S(t) = \sum_{i,j} \varepsilon'_{ij}(t) d_i^\dagger d_j$ with the renormalized energy matrix $\varepsilon'_{ij}(t)$ of the DQDs includes the energy shift of each level and the lead-induced couplings between different levels. The remaining terms give the nonunitary dissipation and fluctuation processes induced by backactions of the electrons from the leads and are described by the dissipation and fluctuation coefficients $\boldsymbol{\gamma}(t)$ and $\widetilde{\boldsymbol{\gamma}}(t)$, respectively. Explicitly, all the time-dependent coefficients in Eq. (A1) are found to be

$$\boldsymbol{\varepsilon}'(t) = \frac{1}{2}[\dot{\boldsymbol{u}}(t, t_0)\boldsymbol{u}^{-1}(t, t_0) - \text{H.c.}], \quad \text{(A2a)}$$

$$\boldsymbol{\gamma}(t) = -\frac{1}{2}[\dot{\boldsymbol{u}}(t, t_0)\boldsymbol{u}^{-1}(t, t_0) + \text{H.c.}], \quad \text{(A2b)}$$

$$\widetilde{\boldsymbol{\gamma}}(t) = \dot{\boldsymbol{v}}(t, t) - [\dot{\boldsymbol{u}}(t, t_0)\boldsymbol{u}^{-1}(t, t_0)\boldsymbol{v}(t, t) + \text{H.c.}], \quad \text{(A2c)}$$

where functions $\boldsymbol{u}(\tau, t_0)$ and $\boldsymbol{v}(\tau, t)$ satisfy the following integro-differential equations [30–32],

$$\frac{d}{d\tau}\boldsymbol{u}(\tau, t_0) + \frac{i}{\hbar}\boldsymbol{\varepsilon}\boldsymbol{u}(\tau, t_0) + \sum_\alpha \int_{t_0}^\tau d\tau' \boldsymbol{g}_\alpha(\tau, \tau')\boldsymbol{u}(\tau', t_0) = 0,$$
$$\text{(A3a)}$$

$$\frac{d}{d\tau}\boldsymbol{v}(\tau, t) + \frac{i}{\hbar}\boldsymbol{\varepsilon}\boldsymbol{v}(\tau, t) + \sum_\alpha \int_{t_0}^\tau d\tau' \boldsymbol{g}_\alpha(\tau, \tau')\boldsymbol{v}(\tau', t)$$
$$= \sum_\alpha \int_{t_0}^t d\tau' \widetilde{\boldsymbol{g}}_\alpha(\tau, \tau')\boldsymbol{u}^\dagger(t, \tau'), \quad \text{(A3b)}$$

subject to the boundary conditions $\boldsymbol{u}(t_0,t_0) = \mathbf{1}$ and $\boldsymbol{v}(t_0,t) = \mathbf{0}$. In the above equations, the time nonlocal integral kernels, $\boldsymbol{g}_\alpha(\tau,\tau')$ and $\widetilde{\boldsymbol{g}}_\alpha(\tau,\tau')$ characterizing all the memory effects between the dots and lead α are defined as

$$\boldsymbol{g}_\alpha(\tau,\tau') = \int \frac{d\omega}{2\pi} \boldsymbol{\Gamma}_\alpha(\omega) e^{-i\omega(\tau-\tau')}, \tag{A4a}$$

$$\widetilde{\boldsymbol{g}}_\alpha(\tau,\tau') = \int \frac{d\omega}{2\pi} \boldsymbol{\Gamma}_\alpha(\omega) f_\alpha(\omega) e^{-i\omega(\tau-\tau')}, \tag{A4b}$$

where $\boldsymbol{\Gamma}_\alpha(\omega)$ is the spectral density (level broadening) of lead α,

$$\Gamma_{\alpha ij}(\omega) = 2\pi \sum_k V_{i\alpha k} V^*_{j\alpha k} \delta(\omega - \epsilon_{\alpha k}), \tag{A5}$$

and $f_\alpha(\omega) = 1/(e^{\beta(\omega-\mu_\alpha)} + 1)$ is the Fermi-Dirac distribution function of lead α at initial time t_0, and $\beta = 1/k_B T$, the inverse temperature. Solving the inhomogeneous equation (A3b) with the initial condition $\boldsymbol{v}(t_0,t) = \mathbf{0}$, one obtains,

$$\boldsymbol{v}(\tau,t) = \sum_\alpha \int_{t_0}^\tau d\tau_1 \int_{t_0}^t d\tau_2 \boldsymbol{u}(\tau,\tau_1) \widetilde{\boldsymbol{g}}_\alpha(\tau_1,\tau_2) \boldsymbol{u}^\dagger(t,\tau_2). \tag{A6}$$

In fact, $\boldsymbol{u}(\tau,t_0)$ and $\boldsymbol{v}(\tau,t)$ are related to the retarded Green function and the lesser Green function of the device system in the nonequilibrium Green function techniques [33–35], and Eq. (A6) gives the generalized nonequilibrium fluctuation-dissipation theorem in the time domain [42].

Also, one can obtain the reduced density matrix $\rho(t)$. Denoting the empty state with $|0\rangle$, the state that one electron occupied in dot i with $|i\rangle$ ($i = 1,2$), and the doubly occupied state by $|d\rangle$, the elements of reduced density matrix at the later time t for an arbitrary initial DQD state that obey the master equation (A1), can be expressed as follows [36],

$$\rho_{00}(t) = A(t) \left\{ \rho_{00}(t_0) + \rho_{dd}(t_0) \det[\boldsymbol{J}_3(t)] \right.$$
$$\left. - \sum_{i,j} \rho_{ij}(t_0) \boldsymbol{J}_{3ji}(t) \right\}, \tag{A7a}$$

$$\rho_{11}(t) = 1 - \rho_{00}(t) - \rho_{22}^{(1)}(t), \rho_{12}(t) = \rho_{12}^{(1)}(t), \tag{A7b}$$

$$\rho_{22}(t) = 1 - \rho_{00}(t) - \rho_{11}^{(1)}(t), \rho_{21}(t) = \rho_{12}^{*(1)}(t), \tag{A7c}$$

$$\rho_{dd}(t) = 1 - \rho_{00}(t) - \rho_{11}(t) - \rho_{22}(t), \tag{A7d}$$

while the other off-diagonal density matrix elements between the different states are all zero. The coefficients in Eq. (A7) are $A(t) = \det[\mathbf{1} - \boldsymbol{v}(t,t)]$, $\boldsymbol{J}_3(t) = \boldsymbol{u}^\dagger(t,t_0)[\mathbf{1} - \boldsymbol{v}(t,t)]^{-1}\boldsymbol{u}(t,t_0) - \mathbf{1}$, and $\rho(t_0)$ is the initial reduced density matrix. The single-particle correlation function $\rho_{ij}^{(1)}(\tau,t) = \langle a_j^\dagger(t) a_i(\tau)\rangle$ is solved explicitly in Refs. [30–32],

$$\rho_{ij}^{(1)}(\tau,t) = [\boldsymbol{u}(\tau,t_0)\boldsymbol{\rho}^{(1)}(t_0)\boldsymbol{u}^\dagger(t,t_0) + \boldsymbol{v}(\tau,t)]_{ij}, \tag{A8}$$

where $\rho_{ij}^{(1)}(t_0) = \rho_{ij}^{(1)}(t_0,t_0)$ is the initial single-particle density matrix. In fact, it is easy to obtain the solution of the reduced density matrix Eq. (A7). Specifically, Eq. (A7d) is a direct consequence of $\mathrm{Tr}[\rho(t)] = 1$. Then, by definition, one has $\rho_{ii}(t) = \rho_{ii}^{(1)}(t) - \rho_{dd}(t)$ for $i = 1,2$ and $\rho_{ij}(t) = \rho_{ij}^{(1)}(t)$ for $i \neq j$, combining which with Eq. (A7d) gives directly the solutions of Eqs. (A7b) and (A7c). The solution of Eq. (A7a) is a little bit difficult to find; it was calculated from $\rho_{00}(t) = \langle 0|\rho(t)|0\rangle = \langle 0|\mathrm{Tr}_E[\rho_{\mathrm{tot}}(t)]|0\rangle$ by using the path integral approach Refs. [30,31], but it is easy to check that the solution of Eq. (A7a) satisfies the master equation Eq. (A1).

On the other hand, the transient transport current of electrons flowing from lead α into the DQDs is defined as

$$I_\alpha(t) = -e \frac{d}{dt} \mathrm{Tr}_{S\otimes E}[\rho_{\mathrm{tot}}(t) N_\alpha], \tag{A9}$$

where $N_\alpha = \sum_k c_{\alpha k}^\dagger c_{\alpha k}$ is the total electron number in lead α. Using the master equation approach, the transport current can also be expressed in terms of the same Green functions of the DQDs, $\boldsymbol{u}(\tau,t_0)$ and $\boldsymbol{v}(\tau,t)$, as follows [30–32]:

$$I_\alpha(t) = -\frac{2e}{\hbar} \mathrm{Re} \int_{t_0}^t \mathrm{Tr}[\boldsymbol{g}_\alpha(t,\tau)\boldsymbol{\rho}^{(1)}(\tau,t) - \widetilde{\boldsymbol{g}}_\alpha(t,\tau)\boldsymbol{u}^\dagger(t,\tau)]. \tag{A10}$$

Indeed, the transient transport current (A10) obtained from our master equation approach has exactly the same form as that in the time-dependent transport theory developed by Wingreen, Jauho, and Meir based on the nonequilibrium Green function technique [33–35]. It is worth noting that in Refs. [33–35] the initial-state dependence of the DQD system, i.e., the first term in Eq. (A8), was omitted, because Keldysh's nonequilibrium Green function technique usually starts the initial time from the minus infinity ($t_0 \to -\infty$) which oversimplifies the initial-state dependence in the transient quantum transport dynamics.

Furthermore, in the wide band limit considered in this paper, the transient net current, $I(t) = 1/2[I_L(t) - I_R(t)]$, is given explicitly as follows,

$$I(t) = -\frac{e}{\hbar} \mathrm{Re}\,\mathrm{Tr}\left\{ \frac{1}{2}(\boldsymbol{\Gamma}_L - \boldsymbol{\Gamma}_R)\left[\boldsymbol{u}(t,t_0)\boldsymbol{\rho}^{(1)}(t_0)\boldsymbol{u}^\dagger(t,t_0) + \int_{t_0}^t d\tau_1 \int_{t_0}^t d\tau_2 \boldsymbol{u}(t,\tau_1) \int \frac{d\omega}{2\pi} [\boldsymbol{\Gamma}_L f_L(\omega) + \boldsymbol{\Gamma}_R f_R(\omega)] e^{-i\omega(\tau_1-\tau_2)} \boldsymbol{u}^\dagger(t,\tau_2) \right] \right.$$
$$\left. - \int_{t_0}^t d\tau \int \frac{d\omega}{2\pi} [\boldsymbol{\Gamma}_L f_L(\omega) - \boldsymbol{\Gamma}_R f_R(\omega)] \boldsymbol{u}^\dagger(t,\tau) e^{-i\omega(t-\tau)} \right\}. \tag{A11}$$

Here the first term is the initial-state dependence of the DQD system in the transient transport current [30–32]. However, this initial-state dependence is independent of the bias voltage $V = (\mu_L - \mu_R)/e$ initially applied to the leads. Therefore, the derivative of the net current with respect to the bias voltage results in the transient linear conductance being DQD initial-state independent, as given explicitly by Eq. (8).

[1] U. Fano, Phys. Rev. **124**, 1866 (1961).

[2] A. E. Miroshnichenko, S. Flach, and Y. S. Kivshar, Rev. Mod. Phys. **82**, 2257 (2010).

[3] G. Breit and E. Wigner, Phys. Rev. **49**, 519 (1936).

[4] M. Wickenhauser, J. Burgdörfer, F. Krausz, and M. Drescher, Phys. Rev. Lett. **94**, 023002 (2005).

[5] A. Kaldun, A. Blättermann, V. Stooß, S. Donsa, H. Wei, R. Pazourek, S. Nagele, C. Ott, C. D. Lin, J. Burgdörfer, and T. Pfeifer, Science **354**, 738 (2016).

[6] W. Lu, Z. Ji, L. Pfeiffer, K. W. West, and A. J. Rimberg, Nature (London) **423**, 422 (2003).

[7] J. Bylander, T. Duty, and P. Delsing, Nature (London) **434**, 361 (2005).

[8] S. Gustavsson, I. Shorubalko, R. Leturcq, S. Schön, and K. Ensslin, Appl. Phys. Lett. **92**, 152101 (2008).

[9] J. Güttinger, J. Seif, C. Stampfer, A. Capelli, K. Ensslin, and T. Ihn, Phys. Rev. B **83**, 165445 (2011).

[10] M. A. Kastner, Phys. Today **46**(1), 24 (1993).

[11] J. Göres, D. Goldhaber-Gordon, S. Heemeyer, M. A. Kastner, H. Shtrikman, D. Mahalu, and U. Meirav, Phys. Rev. B **62**, 2188 (2000).

[12] I. G. Zacharia, D. Goldhaber-Gordon, G. Granger, M. A. Kastner, Y. B. Khavin, H. Shtrikman, D. Mahalu, and U. Meirav, Phys. Rev. B **64**, 155311 (2001).

[13] A. C. Johnson, C. M. Marcus, M. P. Hanson, and A. C. Gossard, Phys. Rev. Lett. **93**, 106803 (2004).

[14] Y. Aharonov and D. Bohm, Phys. Rev. **115**, 485 (1959).

[15] K. Kobayashi, H. Aikawa, S. Katsumoto, and Y. Iye, Phys. Rev. Lett. **88**, 256806 (2002).

[16] K. Kobayashi, H. Aikawa, S. Katsumoto, and Y. Iye, Phys. Rev. B **68**, 235304 (2003).

[17] J. Kim, J.-R. Kim, J.-O. Lee, J. W. Park, H. M. So, N. Kim, K. Kang, K.-H. Yoo, and J.-J. Kim, Phys. Rev. Lett. **90**, 166403 (2003).

[18] A. W. Holleitner, C. R. Decker, H. Qin, K. Eberl, and R. H. Blick, Phys. Rev. Lett. **87**, 256802 (2001).

[19] T. Hatano, M. Stopa, W. Izumida, T. Yamaguchi, T. Ota, and S. Tarucha, Physica E (Amsterdam) **22**, 534 (2004).

[20] M. Sigrist, A. Fuhrer, T. Ihn, K. Ensslin, S. E. Ulloa, W. Wegscheider, and M. Bichler, Phys. Rev. Lett. **93**, 066802 (2004).

[21] B. Kubala and J. König, Phys. Rev. B **65**, 245301 (2002).

[22] M. L. L. de Guevara, F. Claro, and P. A. Orellana, Phys. Rev. B **67**, 195335 (2003).

[23] K. Kang and S. Y. Cho, J. Phys.: Condens. Matter **16**, 117 (2004).

[24] Z.-M. Bai, M.-F. Yang, and Y.-C. Chen, J. Phys.: Condens. Matter **16**, 2053 (2004).

[25] H. Lu, R. Lü, and B. F. Zhu, Phys. Rev. B **71**, 235320 (2005).

[26] T. Kubo, Y. Tokura, T. Hatano, and S. Tarucha, Phys. Rev. B **74**, 205310 (2006).

[27] B. Dong, I. Djuric, H. L. Cui, and X. L. Lei, J. Phys.: Condens. Matter **16**, 4303 (2004).

[28] R. López, D. Sánchez, M. Lee, M.-S. Choi, P. Simon, and K. Le Hur, Phys. Rev. B **71**, 115312 (2005).

[29] M. A. Sierra, M. Saiz-Bretín, F. Domínguez-Adame, and D. Sánchez, Phys. Rev. B **93**, 235452 (2016).

[30] M. W.-Y. Tu and W.-M. Zhang, Phys. Rev. B **78**, 235311 (2008).

[31] J. S. Jin, M. W.-Y. Tu, W.-M. Zhang, and Y. J. Yan, New J. Phys. **12**, 083013 (2010).

[32] P. Y. Yang and W. M. Zhang, Front. Phys. **12**, 127204 (2017).

[33] H. Haug and A. P. Jauho, *Quantum Kinetics in Transport and Optics of Semiconductors*, Springer Series in Solid-State Sciences, Vol. 123 (Springer-Verlag, Berlin, 2008).

[34] N. S. Wingreen, A.-P. Jauho, and Y. Meir, Phys. Rev. B **48**, 8487(R) (1993).

[35] A.-P. Jauho, N. S. Wingreen, and Y. Meir, Phys. Rev. B **50**, 5528 (1994).

[36] J.-H. Liu, M. W.-Y. Tu, and W.-M. Zhang, Phys. Rev. B **94**, 045403 (2016).

[37] M. W.-Y. Tu, W.-M. Zhang, J. S. Jin, O. Entin-Wohlman, and A. Aharony, Phys. Rev. B **86**, 115453 (2012).

[38] M. W.-Y. Tu, A. Aharony, O. Entin-Wohlman, A. Schiller, and W.-M. Zhang, Phys. Rev. B **93**, 125437 (2016).

[39] A. Yacoby, M. Heiblum, D. Mahalu, and H. Shtrikman, Phys. Rev. Lett. **74**, 4047 (1995).

[40] A. Yacoby, R. Schuster, and M. Heiblum, Phys. Rev. B **53**, 9583 (1996).

[41] J. S. Jin, S. K. Wang, J. H. Zhou, W.-M. Zhang, Y. J. Yan, arXiv:1706.06500.

[42] W.-M. Zhang, P.-Y. Lo, H.-N. Xiong, M. W.-Y Tu, and F. Nori, Phys. Rev. Lett. **109**, 170402 (2012).